JOURNAL OF CATALYSIS 152, 275–290 (1995)

The Nature of NiMo Phases Encaged in HY Zeolites

J. Leglise,* J. M. Manoli,† C. Potvin,† G. Djega-Mariadassou,† and D. Cornet*,[1]

*Laboratoire Catalyse et Spectrochimie, URA CNRS 0414, I.S.M.Ra., Université de Caen, 6 Bd. Maréchal Juin, F-14050 Caen Cedex, France; and †Laboratoire Réactivité de Surface, URA CNRS 1106, Université P. & M. Curie, 4 Place Jussieu, F-75252 Paris Cedex 05, France

Received February 9, 1994; revised October 18, 1994

NiMo sulfide combined with an acidic HY zeolite constitutes a bifunctional catalyst which may be used in alkane hydroconversion. In this work the distribution of Ni and Mo ions loaded in two HY zeolites (HY-3 and HY-17, with Si/Al = 3 and 17, respectively) is examined by transmission electron microscopy, energy dispersive X-ray spectroscopy, X-ray diffraction, and N_2 adsorption. With zeolite HY-3, all the Ni but only half the Mo is found inside the grains, mainly in the cavities; MoO_3 microcrystals are observed outside the grains. Sulfidation transforms the outer part of the MoO_3 crystals into MoS_2, but small MoS_2-like particles (7 to 15 nm long, 3 slabs thick) are also detected inside the zeolite, mostly in the secondary pores. No significant migration of Mo occurs, but only 50% of the Ni is retained in the sulfided zeolite. Zeolite HY-17 is able to accommodate all the Ni and Mo ions, mainly in the large mesoporous volume. Sulfidation evicts 50% of Ni and ca. 30% of Mo from the zeolite particles. Again, MoS_2-like entities (30 to 40 nm large, 6 to 10 slabs thick) are observed inside the grains. The dispersion of the NiMo sulfide in the HY-17 zeolite appears to be higher than in the HY-3 support. The NiMoY catalysts were evaluated for the simultaneous hydrogenation of benzene and hydroconversion of *n*-heptane. Owing to the good dispersion and accessibility of the NiMo sulfide, the zeolite catalysts are as active as $NiMo/Al_2O_3$ for hydrogenation. This hydrogenation activity, however, is unable to impart an adequate selectivity in hydroconversion of heptane.

INTRODUCTION

NiMo sulfide is often associated with a HY zeolite in the composition of hydrocracking catalysts (1, 2). The selectivity of such bifunctional catalysts, i.e., the balance between cracking and isomerization, is determined by (i) the relative number of hydrogenating (NiMo) and acidic (OH) centers, (ii) their specific activity, and (iii) their mutual separation. Moreover, the rate of coke formation depends on the spatial distribution of the various sites.

Simple mixtures of HY zeolite and $NiMo/Al_2O_3$ may not have an optimal hydrogenation function, and furthermore their NiMo and OH sites are far apart. Thus the level of cracking is likely to be excessive. However, NiMo sulfide is easily built up in zeolite HY, and it was anticipated that such a catalyst would be more selective for alkane isomerization.

Previous measurements carried out with a series of NiMo/HY zeolites (3–5) revealed that the rate of *n*-heptane hydroconversion strongly increased with Al content (framework or nonframework), whereas the rate of hydrogenation of benzene changed comparatively little. The conversion of heptane over all these catalysts was largely oriented toward cracking. Therefore, the dispersion of NiMo in zeolite HY may be questioned.

In the present work, two NiMo zeolites with different Si/Al ratios are examined by transmission electron microscopy (TEM) coupled with local analysis by energy dispersive X-ray spectroscopy (EDX). TEM is frequently used to examine Mo-based hydrotreating catalysts (6–16). In most instances, Mo appears to be well dispersed over alumina and similar supports, and particles of MoS_2 are evidenced by characteristic fringes (6, 7). In favorable cases, the flake-shaped particles are about 2 to 8 nm long and 1 to 3 layers thick, but larger sizes have been reported, depending on Mo content and sulfiding temperature (8–10). No phase containing the promoter (Ni or Co) has been identified by TEM (11), although these ions were detected by EDX (12, 13). On the zeolite carrier, the dispersion of Mo may be affected by the presence of small internal channels. In a previous IR study, hydroxyl bands were not found in Mo/HY, either calcined or sulfided, showing that Mo ions interact with the zeolite framework (17). In the present study, combined TEM and EDX will be used to specify the nature of Ni and Mo species in NiMo/HY catalysts. Their location, inside or at the surface of the zeolite grains, will be especially examined. The TEM results will be complemented by measuring X-ray crystallinities and internal volumes.

[1] To whom correspondence should be addressed.

0021-9517/95 $6.00

TABLE 1

Chemical Composition of Zeolite Catalysts

Catalyst	R = Si/Al[a] (lattice)	Composition (at.%)[b]				
		Si	Al	Ni	Mo	S
NaY	2.5	71.2	28.8	0	0	0
NiMo(9)NaY	2.2	63.9	25.9	3.4	6.8	0
HY-3	5.0	75.0	25.0	0	0	0
NiMo(5)Y-3	5.5	70.8	23.6	2.8	2.8	0
NiMo(9)Y-3	4.5	68.4	22.8	2.9	5.9	0
NiMo(20)Y-3	6.1	63.3	21.1	1.8	13.8	0
NiMo(9)S_lY-3	5.6	64.5	21.5	2.7	5.4	5.9
NiMo(9)S_hY-3	7.0	64.5	21.5	2.6	5.3	6.1
HY-17	17.4	94.4	5.6	0	0	0
NiMo(10)Y-17	34.5	85.9	5.1	2.4	6.6	0
NiMo(10)S_lY-17	41.4	80.0	4.7	2.3	6.2	6.8
NiMo(10)S_hY-17	41.0	78.9	4.6	2.2	6.1	8.2

[a]Determined by IR.
[b]Excluding oxygen, sodium, carbon, and hydrogen.

EXPERIMENTAL

1. Catalysts

Three Y zeolites, with various acidities, were loaded with NiMo: these were NaY (Linde LZY 52); HY-3 with overall Si/Al = 3, which was a stabilized Y (LZY 82); and finally HY-17 with overall Si/Al = 17, which was obtained by steaming NH_4Y (LZY 62) at 1013 K, followed by washing with 3 M HCl.

Nickel was introduced in HY-3 by ion exchange at 298 K with an aqueous solution of Ni^{2+}; for HY-17, the excess solution had to be evaporated by boiling. Molybdenum was then loaded by filling the zeolite pores with the minimum amount of ammonium heptamolybdate solution (3). The samples are designated as NiMo(x)Y, where x indicates the amount of Mo (in weight percent) in the dry solid.

The catalysts were calcined at 773 K, and then samples of ca. 0.16 g were sulfided at either 593 K (low temperature, samples denoted S_l) or 673 K (high temperature, S_h). Sulfidation was performed with a flow of hydrogen containing heptane (Hp, 0.45 vol.%), benzene (Be, 0.15 vol.%), and dimethyldisulfide (DMDS, 0.012 vol.%). The gas flow rate was 6 liter h^{-1}, and the total pressure was 8 MPa.

Metal contents were determined by atomic absorption (C.N.R.S. Analytical Division, Vernaison). The compositions (Si, Al, Ni, Mo, S) are given in Table 1 as normalized atom percentages, i.e., excluding oxygen, sodium, carbon and hydrogen; this facilitates comparison with the EDX data.

The Si/Al ratio R in the zeolite framework was estimated from the IR spectra of the powders diluted with KBr (Nicolet MX1 spectrometer). Table 1 reports the R values deduced from the position of the lattice vibrations ν_a around 1080 cm^{-1} (18). They are rather insensitive to the presence of cations, including nonframework Al.

2. Catalytic Measurements

The reaction of n-heptane and benzene with hydrogen was carried out at 500–600 K over the sulfided NiMoSY catalysts. The high pressure reactor (8 MPa) contained 0.2 to 0.6 g of catalyst. The reactant was the Hp–Be–DMDS mixture (78–20–2 wt.%) already used for sulfidation. The feed rate was 0.16 g h^{-1}, so that all reagents were gaseous. Partial pressures were 12 kPa for Be and 37 kPa for Hp. Details may be found elsewhere (4).

3. X-Ray Characterization and Sorption Capacity

The X-ray powder patterns were recorded on a Philips PW 1390 diffractometer using Cu$K\alpha$ radiation. The unit-cell parameter of the zeolites was determined by a full pattern matching procedure.

The crystalline fraction C_e, defined as the percent XRD intensity relative to NaY, was determined according to the ASTM method (19). As the catalysts contain amorphous Mo and Ni phases, the experimental crystallinities C_e(NiMoY) must be corrected to assess the intrinsic crystallinity C_i(Y) of the silico–aluminate fraction. The main correction arises from MoO_3 since Mo has the largest weight absorption coefficient (20).

Hence C_i was calculated according to the formula

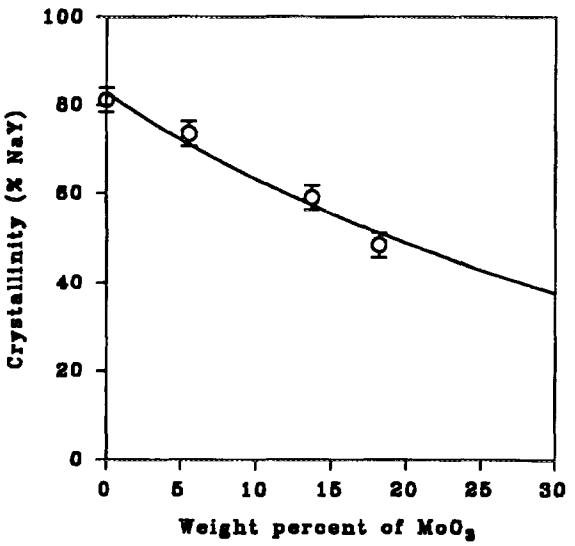

FIG. 1. Variation in X-ray diffraction intensity of zeolite HY-3 (relative to NaY) versus amount of MoO_3, for mixtures of HY-3 and MoO_3.

$$C_e(\text{NiMoY}) = C_i(\text{Y})\frac{1-w}{1+(\rho-1)w},$$

where ρ is the weight absorption coefficient of MoO_3 relative to that of hydrated HY, and w is the weight fraction of MoO_3. To evaluate ρ, the crystallinities of three mechanical mixtures of HY-3 and MoO_3 were measured. The best fit was found at $\rho = 2.8$ (Fig. 1). This value was retained to determine the C_i. No such corrections were attempted for nickel and sulfur.

Nitrogen sorption was measured at 77 K with a Micromeritics ASAP 2000 apparatus. The total pore volume V_{tot} was obtained from nitrogen uptake at a relative pressure $p/p_0 = 0.98$, whereby all pores under 94 nm diameter were filled. Micropore volume (V_{mic}) was derived from the intercept of the linear portion of the t-plots in the range of thickness $0.6 < t < 0.9$ nm (21). The secondary pore (or mesopore) volume V_{sec} was obtained as the difference between V_{tot} and V_{mic}.

4. Electron Microscopy

Zeolite grains to be studied by STEM-EDX or by TEM were dispersed in pure ethanol; the suspension was stirred in an ultrasonic bath and one drop was placed on a carbon-coated copper grid. Thin cuts of the powder were also produced by embedding the catalysts in an epoxy resin and cutting them with an ultramicrotome equipped with a diamond knife (thin sections: 80–100 nm).

The specimens were studied using a JEOL (JEM 100CXII) transmission scanning electron microscope equipped with a scanning device ASID 4D (STEM mode). The operating voltage was 100 kV. EDX analyses were performed using a LINK AN10000 system connected to a silicon–lithium diode detector and a multichannel analyzer. The X-rays emitted from the specimen upon electron impact were collected in the range 0–20 keV for 400 s. The EDX analyses were obtained either from relatively large domains (150×200 nm^2 to 400×533 nm^2) or from smaller domains (punctual-STEM beam analyses: 177 or 1256 nm^2). Atomic compositions c (%) were obtained using the standard ratio thin section 2 LINK program (RTS-2/FLS). Since the Mo_L and S_K lines overlap, the determination of Mo in the sulfided catalysts relied on the intensity of Mo_K. The intensity $I(S_K)$ could then be determined by subtracting the contribution $I(Mo_L) = 3.66\, I(Mo_K)$.

High resolution (HREM) observations and selected area electron diffraction (SAED) were performed with a JEOL apparatus (JEM 100CXII) equipped with a top-entry device and operating at 100 kV.

RESULTS

1. Zeolite Framework Composition

Contacting the Y zeolites with Ni and Mo solutions, followed by calcination, may extract some Al from the lattice, and create amorphous zones (22, 23). Further defects may be created by the sulfidation procedure (24, 25).

Inspection of the IR spectra shows that the position of the ν_a band in NaY did not change after NiMo introduction. Consequently, the lattice ratio Si/Al was not affected (Table 1).

In zeolite HY-3, the lattice ratio determined by IR differed from the bulk ratio (5 ± 0.5 instead of 3), showing the heterogeneity of the material. In NiMo(9)Y-3, the ν_a band was shifted by only 3 cm^{-1} below its position in HY-3 (Fig. 2). Again, this rules out any dealumination of the framework. However, at 20% Mo loading, the same band was shifted 5 cm^{-1} upward. The lattice ratio R increased from 5 to 6 (Table 1), revealing some dealumination.

In the spectrum of NiMo(9)S_lY-3 sulfided at 593 K (Fig. 2) the vibration at 900 cm^{-1} characteristic for Mo–O bonds (17, 22) nearly disappeared. At this stage, the zeolite lattice was not affected. However, dealumination was significant when sulfiding at 673 K, as we found $R = 7$ in sample NiMo(9)S_hY (Table 1).

The highly dealuminated zeolite HY-17 appeared to be more homogeneous with negligible amounts of nonframework Al. Upon loading NiMo to HY-17, the ratio R rose from 17.4 to 34.5 and reached 41 after sulfidation.

2. X-Ray Crystallinity

The X-ray diffraction (XRD) crystallinities C_e relative to NaY appear in Table 2 for the various catalysts. Compared with the bare supports, the intensities of diffraction

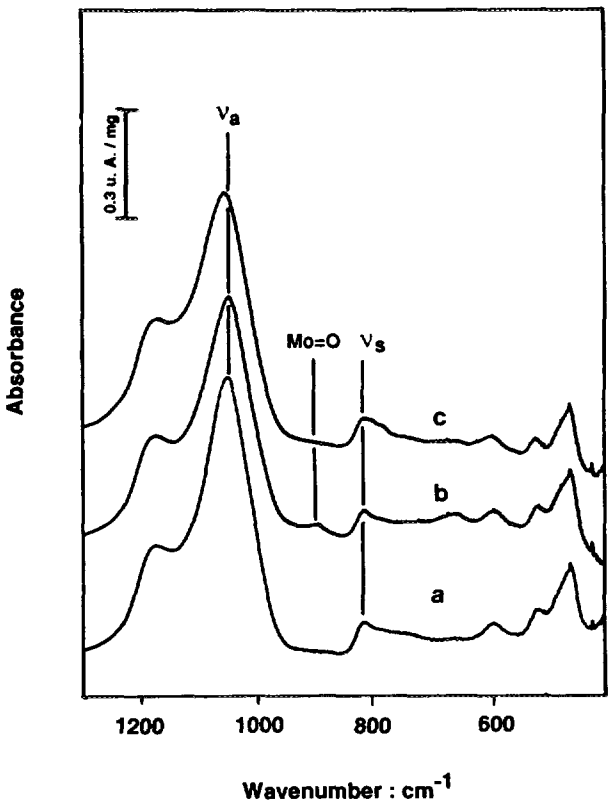

FIG. 2. FT-IR absorption spectra (400–1300 cm^{-1}) of HY-3-based catalysts: HY-3 neat (a), NiMo(9)Y-3 (b), and NiMo(9)S_lY-3 (c).

sharply decreased in NiMo-loaded zeolites. If, however, the amorphous MoO_3 is taken into account, the intrinsic crystallinities C_i of the silico–aluminate generally appear lower than those of the bare supports (Table 2).

Looking at the relative intensities of the (533) and (331) diffraction lines, we see that the ratio I_{533}/I_{331} decreases as the amount of lattice Al decreases. The ratios reported in Table 2 confirmed that HY-3 was not dealuminated at moderate NiMo loading. This agrees with the unchanged crystallinity C_i. Loading with 20 wt.% Mo induced some dealumination along with a 25% loss in crystallinity. With HY-17, the effect was much more pronounced since introducing 10% Mo led to a sizeable dealumination and a 25% amorphization (Table 2).

The unit-cell parameters a_0 of the zeolites were generally unchanged after loading with NiMo (Table 2) at least up to 9 wt.% Mo. The sole exception was zeolite HY-3, where a_0 increased by 0.005 nm with the two metals loaded, while with one metal only a_0 did not change (17). This proves there is a direct interaction between Ni and Mo inside the structural cavities of HY-3.

Upon sulfiding the NiMo(9)Y-3 zeolite, a_0 decreased by 0.006 nm and the intensity ratio I_{533}/I_{331} also decreased. Meanwhile, the crystallinity decreased by about 10%. No such decreases were observed when sulfiding NiMo(10)Y-17.

3. Pore Volumes

The volumes of micropores (V_{mic}) and of secondary pores ($V_{sec} = V_{tot} - V_{mic}$) appear in Table 2. For a valid

TABLE 2

Crystallographic and Porosity Data of Zeolite Catalysts

Catalyst	X-ray diffraction[a]				N_2 Adsorption ($cm^3\ g^{-1}$)[b]	
	C_e (%)	C_i (%)	I_{533}/I_{331}	a_0 (nm)	V_{mic}	V_{sec}
NaY	100	100	1.17	2.467	0.370	0.044
NiMo(9)NaY	77	102	1.20	2.467	0.327	0.045
HY-3	81	81	0.93	2.451	0.260	0.110
NiMo(5)Y-3	66	73	0.96	2.456	0.234	0.086
NiMo(9)Y-3	60	79	0.95	2.455	0.236	0.081
NiMo(20)Y-3	32	60	0.90	2.450	0.144	0.088
NiMo(9)S_lY-3	54	72	0.81	2.449	0.206	0.064
NiMo(9)S_hY-3	54	72	0.79	2.449	0.203	0.075
HY-17	101	101	0.61	2.427	0.305	0.216
NiMo(10)Y-17	55	76	0.49	2.428	0.271	0.226
NiMo(10)S_lY-17	51	73	0.53	2.428	0.245	0.187
NiMo(10)S_hY-17	—	—	—	—	0.250	0.200

[a] C_e is the experimental intensity of diffraction (%, relative to NaY); C_i is the intrinsic crystallinity of the zeolitic part. Uncertainties are ±3% on C_e and C_i, and ±0.001 nm on a_0.

[b] The pore volumes refer to 1 g of silico–aluminate. Uncertainties on volumes are ±0.005 $cm^3\ g^{-1}$.

comparison between the solids, all volumes were expressed on a silico–aluminate basis (SA, crystalline + amorphous).

The micropore volume of NaY, corrected for Na cations, was 0.370 cm^3/(g SA) and decreased by 0.043 cm^3 g^{-1} upon loading with Ni (2.7% by weight) and Mo (9%). The difference is nearly the physical volume of NiO + MoO_3 (0.035 cm^3 g^{-1}). As neither the secondary pore volume nor the crystallinity was changed, the Ni–Mo species have probably penetrated the NaY.

When 2.4 wt.% Ni and 9 wt.% Mo were introduced into HY-3, V_{mic} and V_{sec} both decreased by an equivalent amount (0.025 cm^3 g^{-1}, Table 2). The location of NiMo species, in cavities or mesopores, cannot be ascertained because the loss in total volume was greater than that of NiO + MoO_3. Upon sulfiding zeolite NiMo(9)Y-3 at 593 K, V_{mic} further decreased by 0.03 cm^3 g^{-1}. The volumes did not drop further when sulfiding at 673 K.

In zeolite HY-17, introduction of NiMo lowered V_{mic} by 0.03 cm^3 g^{-1}, while V_{sec} remained constant at 0.22 cm^3 g^{-1}. Upon sulfiding NiMoY-17 at 593 K, both V_{mic} and V_{sec} decreased substantially. The decrease in V_{sec} was more moderate after sulfiding at higher temperature.

4. Identification of NiMo Phases by TEM and STEM-EDX

TEM images were obtained on simply ground catalyst particles to detect NiMo phases outside the zeolite grains and also from ultra-thin cuts to examine the inside of the zeolite. STEM-EDX was performed on several NiMoY samples. Similar compositions were found when analyzing either bulk grains or thin cuts.

Oxidic NiMoY-3. A TEM image of catalyst NiMo(9)Y-3 is shown in Fig. 3a. Zeolite grains may be distinguished, with an average diameter around 500 nm. Fringes observed on well-crystallized zones showed that the grains were made of twinned microcrystals oriented at random. Lighter circular spots represent mesopores with diameters from 15 to 25 nm (26, 27). Some material without fine structure shows up at the junctions between grains.

Very dark nodules, about 20 nm in diameter, appeared to be stuck to the outer part of the zeolite particles or aggregated at junctions. From their diffraction pattern, they were identified as MoO_3. In addition, isolated crystals of MoO_3, with diameter up to 400 nm, were detected in some pictures. Ovoid-shaped particles, with the diffraction pattern of $NiMoO_4$, were found in rare instances. Their diameter was under 20 nm.

According to the morphology of the zone analyzed by EDX, the compositions fell into six categories (Fig. 3b). Zones A and Y were found at the interior of the zeolite; B zones were found at the border of the grains; C, D, and E zones corresponded to dark objects at the outside. Typical averaged compositions $\bar{c}$ are reported in Table 3.

When the electron beam and EDX were focused on a zeolite grain (Fig. 3b), composition A occurred most often. It was similar to the overall composition of the zeolite with a Si/Al ratio equal to 3. In addition, Ni and Mo were found at concentrations ca. 3 at.% each (Table 3). Individual measurements deviated little from the average $\bar{c}$: deviations $\Delta\bar{c}/\bar{c}$ were small for Si (2%), moderate for Al and Ni (8 and 14%, respectively), and large for Mo (44%).

The same A zones were found in thin cuts. There the deviations $\Delta\bar{c}/\bar{c}$ were lower, but the Si/Al ratio amounted to 4.2. Some zones were exceptionally encountered, in which both Ni and Mo were missing. Such zones were designated as Y (Fig. 3b). The Y composition reported in Table 3 also differed from the A composition by having the ratio Si/Al = 2.7. This higher Al content probably revealed internal domains containing many cationic Al species, or regions partly amorphized, but devoid of ion-exchange capacity.

When the electron beam was directed toward the dark nodules, either isolated or aggregated, EDX essentially detected molybdenum (D composition) or Mo combined with nickel (E composition). Low amounts of Al (up to 20 at.%) and Si (5 at.% at most) might appear in D and E compositions, but the SAED pattern clearly identified D zones as MoO_3 and E zones as $NiMoO_4$. D zones occurred more frequently than E zones.

Other compositions were intermediate between the four types just described. For instance, the B composition contained mostly Si and Al (Table 3), with the same ratio Si/Al = 3 as in the whole catalyst. The amount of Ni in B zones was nearly the same as in the A zones, but the amount of Mo was distinctly higher, ranging from 7 to 40 at.%. The B zones (Fig. 3b) presumably correspond to the outer parts of the zeolite upon which the MoO_3 nodules are grafted.

Finally, C zones containing Mo and Al, with Mo/Al = 1.5 to 2.5, and very little Si, were found at places where MoO_3 patches were bound to the zeolite grains. Since the molybdate $Al_2(MoO_4)_3$ was detected by Sanders and Pratt on Mo/Al_2O_3 catalysts (6), C zones were examined by SAED. The patterns were characteristic for MoO_3, so that the C zones contained crystalline MoO_3 associated with amorphous alumina.

Compared with the NiMo(9)Y-3, the highly loaded NiMo(20)Y-3 catalyst looked rather heterogeneous, with many more D and E microcrystals, as well as intermediate B and C zones. The A zones in NiMo(20)Y-3 contained hardly more Mo than the similar ones in NiMo(9)Y-3 (4.3 at.% instead of 3 at.%).

Sulfided NiMo(9)SY-3. The appearance of the zeolite grains was preserved upon sulfiding NiMo(9)Y-3 at either 593 or 673 K. TEM images on thin cuts did not reveal any severe internal damage, despite a 10% loss in crystallinity and micropore volume. All domains analyzed by

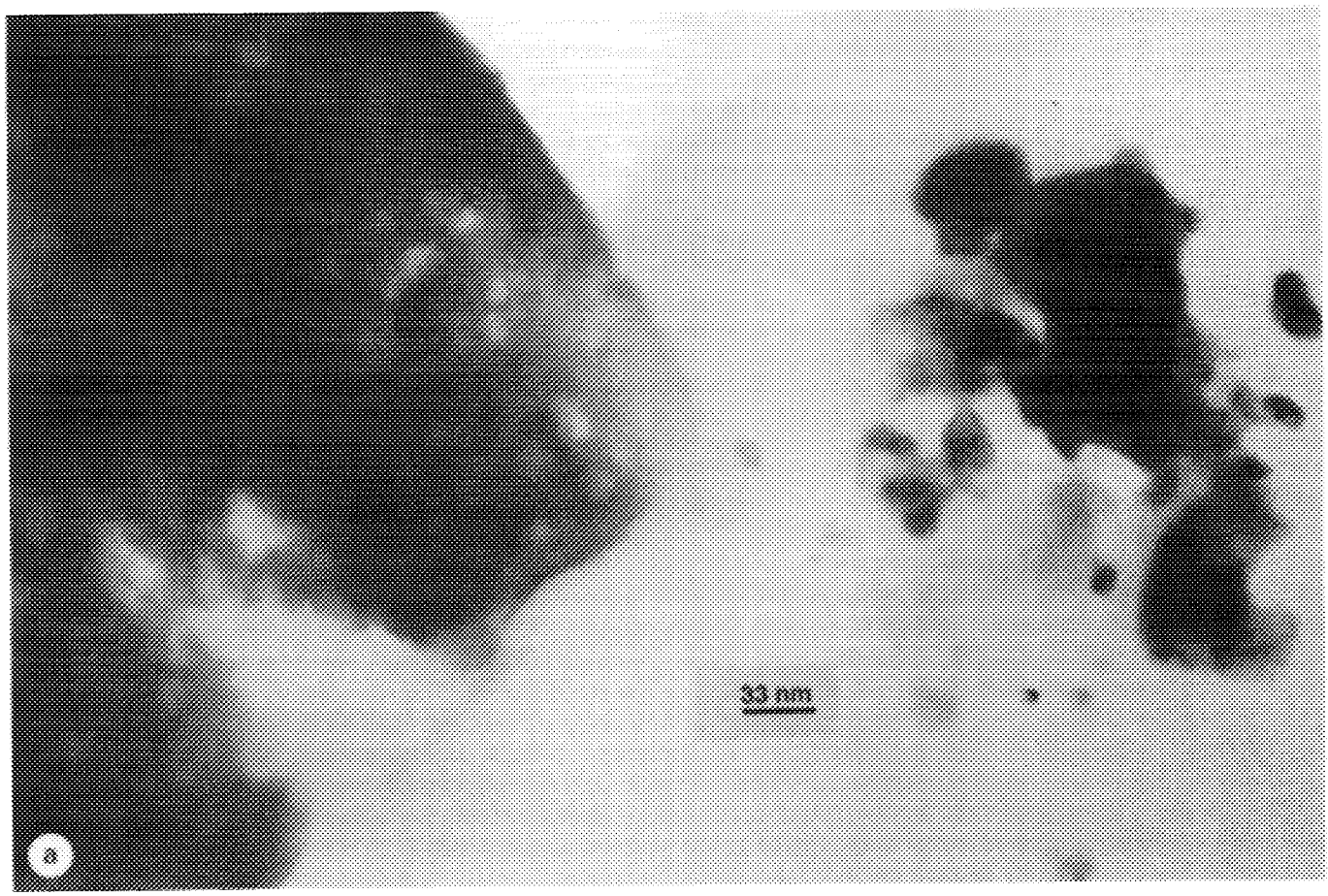

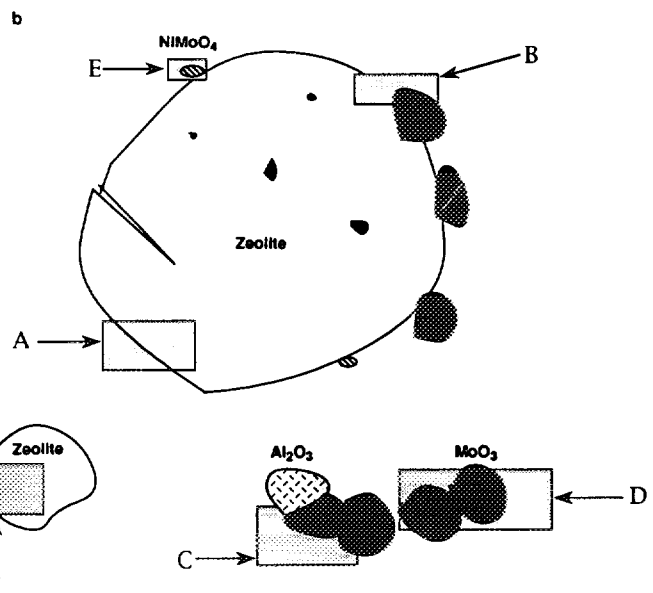

FIG. 3. (a) TEM micrograph of NiMo(9)Y-3 catalyst particles. (b) Characteristic features of the TEM micrographs: shaded rectangles correspond to zones (A to E and Y) mentioned in Table 3. (c) TEM image of a thin section of NiMo(9)Y-3 catalyst.

FIG. 3—*Continued*

EDX contained Ni and Mo. The zeolitic A zones appeared scattered with dark stains, 2 to 15 nm in diameter, and black streaks, 7 to 15 nm long (Fig. 5a). At high magnification, the streaks appeared to be made of one, two, or three parallel fringes. These features were already reported with Mo/Al_2O_3 catalysts (14). The same fringed structure was distinguished on some dark stains (Fig. 5b). Again these fringes with an interlayer spacing of 0.61 nm were characteristic for MoS_2 slabs. Streaks and stains pictured the same entities, i.e., MoS_2 particles, the fringed structure appearing mainly when the (002) planes of MoS_2 were parallel to the electron beam (10, 15).

Upon sulfiding sample NiMo(9)Y-3, the MoO_3 nodules (C and D zones) retained the same general aspect but they were now surrounded by fringes (Fig. 4). The distance between fringes was equal to 0.61 nm, characteristic for MoS_2 (6–8). The outer slabs appeared to be 2–4 fringes thick after sulfiding at 593 K; up to 12 fringes could be distinguished after sulfiding at 673 K. The SAED pattern obtained on the largest nodules revealed MoS_2; the same pattern had been observed on bulk Co–Mo–S catalyst (16).

EDX performed on thin sections showed that, in addition to molybdenum and sulfur, the C nodules contained up to 30 at.% Al and an average of 3 at.% Ni (Table 3). Hence, sulfidation did not change the relative amounts of Mo and Al in the C zones. As shown by the TEM image (Fig. 4) the larger crystals were sulfided only in their outer part. According to Table 3, the atomic S/Mo ratio was between 0.1 and 0.3, so that the cores of the nodules might be reduced to MoO_2 (6).

Although a few needles of $NiMoO_4$ (E zones) were observed in the oxidic precursor, high concentrations of both Ni and Mo were never detected in the sulfided solid. When sulfiding unsupported NiMo catalysts, Sanders and Pratt (6) observed a superficial transformation of $NiMoO_4$ needles, but here the rare E particles apparently disappeared.

Oxidic NiMo(10)Y-17. Zeolite HY-17 exhibited grains with 300 nm average diameter. The contours were irregular and the grains were speckled with clearer spots, revealing a network of oblong-shaped mesopores (d = 30–40 nm). Despite the disordered appearance of the pores, HY-17 was more crystalline than HY-3 and lattice

TABLE 3

EDX Analysis on Various Zones of NiMo(9)Y-3 Catalyst: Comparison of Averaged Compositions $\bar{c}$ with Bulk Chemical Composition

Analysis				Composition (at.%)				
Type	Zone	No. of analyses	Si/Al (at.%/at.%)	Si	Al	Ni	Mo	S
			NiMo(9)Y-3 (calcined at 773 K)					
Chemical			3.0	68.4	22.8	2.9	5.9	0
EDX: grains	A	27	3.4	72.2	21.5	3.0	3.3	0
	B	4	3.1	56.8	18.3	3.9	21.0	0
	C	2	0.6	16.4	29.1	5.7	48.8	0
	D	3	0.7	3.8	5.7	2.9	87.6	0
	E	1	0	0	16.5	31.9	51.6	0
EDX: thin cuts	Y	2	2.7	72.9	26.6	0.3	0.2	0
	A	5	4.2	76.4	18.2	3.0	2.4	0
	B	2	3.5	58.1	16.4	9.8	15.7	0
	C	1	0.2	5.1	29.9	9.8	55.2	0
			NiMo(9)S_lY-3 (sulfided at 593 K)					
Chemical			3.0	64.5	21.5	2.7	5.4	5.9
EDX: thin cuts	A	12	3.5	72.2	20.4	1.3	2.8	3.3
	B	3	3.7	65.9	17.7	1.5	5.5	9.4
	C	4	0.01	0.4	27.9	3.2	52.2	16.3
			NiMo(9)S_hY-3 (sulfided at 673 K)					
Chemical			3.0	64.5	21.5	2.6	5.3	6.1
EDX: thin cuts	A	7	3.3	70.2	21.1	0.9	2.8	5.0
	B	3	2.9	66.8	23.1	1.4	2.9	5.8
	C	1	0.04	1.2	29.9	0.8	59.8	8.3

fringes were clearly distinguished throughout the grains (Fig. 6).

The NiMo(10)Y-17 catalyst contained fewer MoO_3 nodules or patches than NiMo(9)Y-3. $NiMoO_4$ crystals were also less frequent. In EDX analysis, A zones again appeared most often. D and E compositions were also found (Table 4), but Y zones (amorphized domains) were absent, as were B and C zones (MoO_3 + alumina or SA).

Sulfided NiMo(10)SY-17. After sulfidation at 593 K, the zeolite grains appeared scattered with dark stains and streaks (Fig. 7a). The fringes associated with MoS_2 slabs were more clearly resolved than on sulfided NiMoSY-3. The particles were 4–20 nm long, with 3–4 fringes in the smallest ones and 6–10 in the largest. Moreover, the MoS_2 slabs were frequently found at the edge of mesopores; otherwise, they were stuck to the surface of the grains (Fig. 7a).

As with the NiMoY-3 catalysts, the external MoO_3 was sulfided on the surface, and no material arising from sulfidation of $NiMoO_4$ could be detected.

After sulfidation at 673 K, the number of MoS_2 particles increased and their size distribution became broader (Fig. 7b). Many flakes, 4 to 30 nm long, appeared inside the zeolite, while larger particles, 8 to 14 slabs thick, were found at the periphery or at the junction between grains.

5. *Catalytic Activities*

Rates of heptane hydroconversion and benzene hydrogenation measured at 553 K are collected in Table 5. Previous results (4) obtained with catalysts sulfided at 593 K were revised, and data for catalysts sulfided at 673 K were added.

Catalysts NiMoS_lY-3 and NiMoS_lY-17 display similar hydrogenation capacities toward benzene. The rates measured on both catalysts (about 0.05 mol h^{-1} kg^{-1}) are slightly under the value 0.075 measured with a NiMo/Al_2O_3 having similar NiMo content and sulfided in the same way (4).

When the temperature of sulfidation T_S was raised to 673 K, the rate of hydrogenation was nearly doubled for NiMoS_hY-17 and slightly decreased with NiMoS_hY-3. However, the latter catalyst is so acidic that the primary hydrogenation products were cracked to some extent. Then the hydrogenation capacity of NiMoS_hY-3 is difficult to assess, so that the value reported was clearly underestimated.

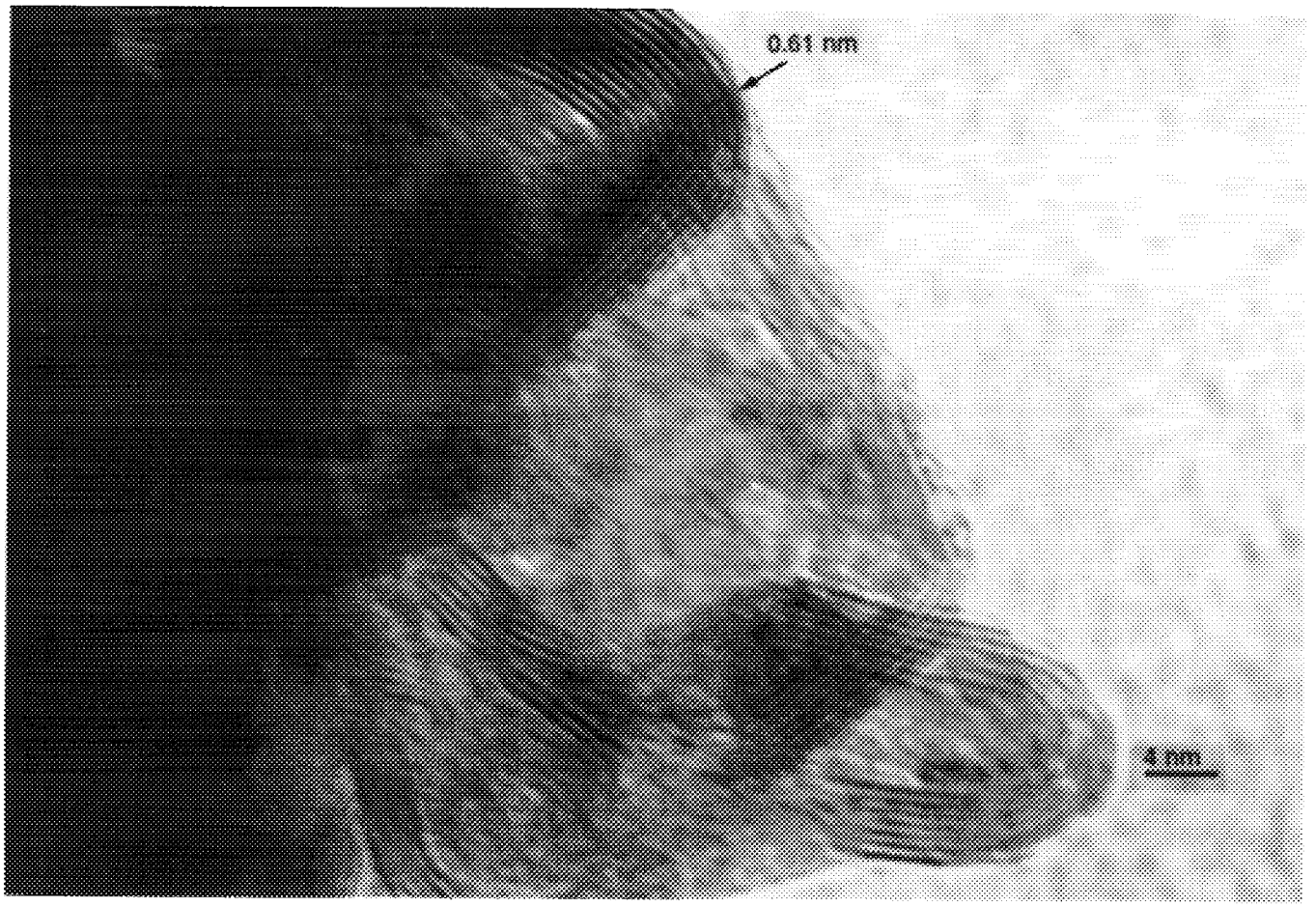

FIG. 4. High magnification of MoO_3 crystals (D zones) surrounded by MoS_2 sheets observed with NiMo(9)S_hY-3 catalyst.

The rates of heptane hydroconversion strongly depend on zeolite composition, the catalyst with a higher Al content being much more active whatever the sulfidation temperature. Raising T_S enhanced the rates of hydroconversion on catalysts with either the Y-3 or the Y-17 support. Turnover frequencies were derived from the numbers of lattice Al in the zeolite supports. Interestingly, they were rather similar on both catalysts (Table 5).

Selectivity in alkane hydroconversion is commonly estimated by the maximum amount of isomers. This maximum was determined at similar temperatures for the two catalysts sulfided at 593 K. With the heptane + benzene feed, we found at most 13% heptane isomers for NiMoY-3 and 10% for NiMoY-17.

DISCUSSION

1. Zeolite Structure and Texture

X-ray crystallinity and N_2 sorption data (Table 2) indicate how much support HY-3 was damaged because of steaming. Compared with NaY, the micropore volume is down by 30%, and the crystallinity by 19% only. This suggests a partial filling of the HY-3 cavities by nonframework aluminum species. In addition, an Al-rich amorphous phase was detected in this solid by EDX (26) and by NMR (28). On the other hand, the increased V_{sec} is probably due to the formation of secondary pores and surface cracks (29).

Zeolite HY-17 with a uniform Al composition and high crystallinity is nearly devoid of any amorphous section. The oblong-shaped mesopores undoubtedly contributed to the large secondary pore volume reported in Table 2. However, V_{sec} also included many necklines at the periphery of the grains. The low V_{mic} is not in line with the 101% crystallinity.

Zeolites NaY, HY-3, and HY-17 reacted differently toward NiMo introduction. IR and crystallinity data (Tables 1 and 2) prove that NaY was able to accommodate up to 15% by weight of Ni and Mo oxides and still remained highly crystalline. Similarly, neither lattice dealumination nor amorphization was evidenced in

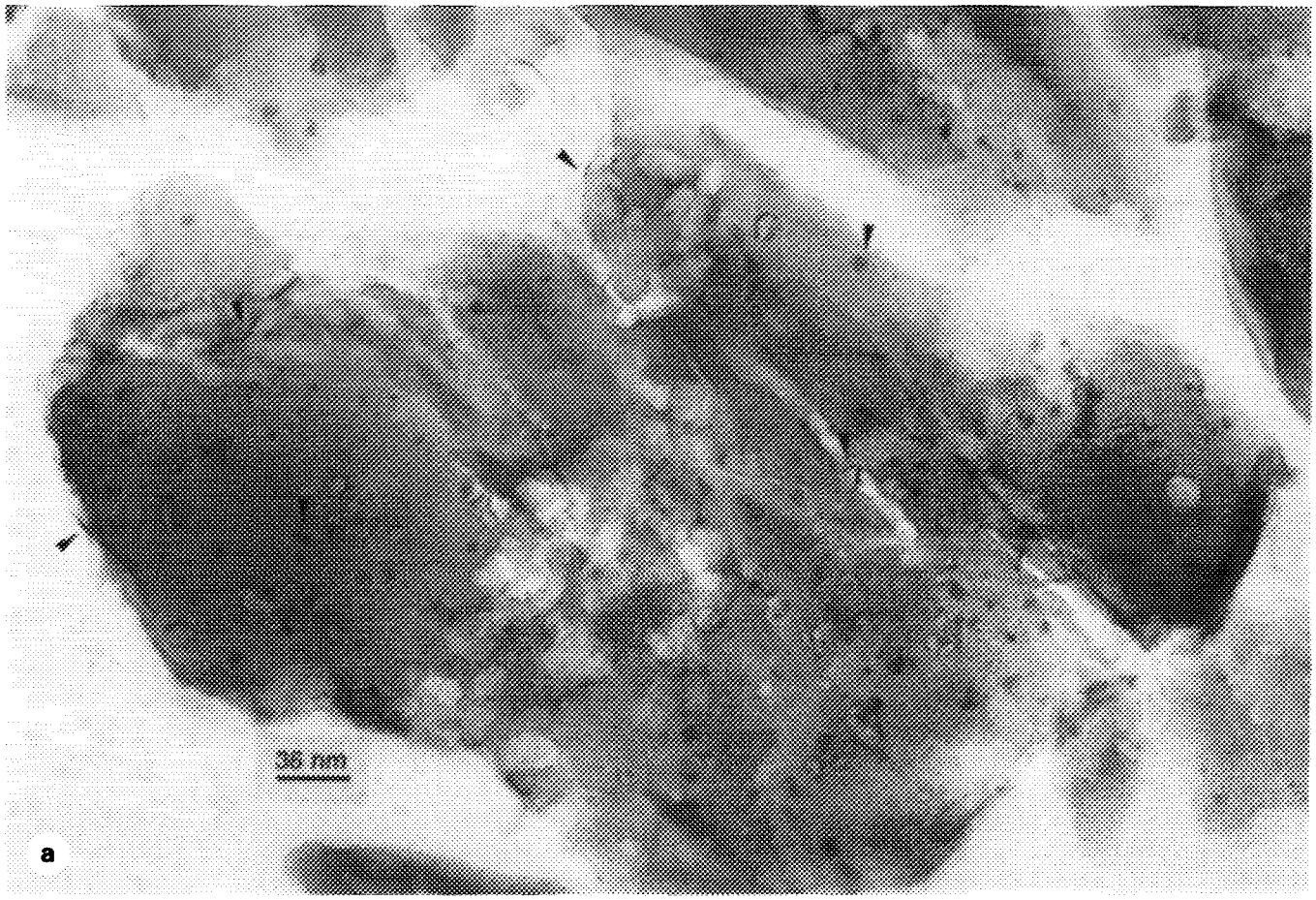

FIG. 5. TEM images of thin cuts in catalysts: (a) NiMo(9)S_lY-3 (sulfided at 593 K); (b) NiMo(9)S_hY-3 (sulfided at 673 K). Arrowheads indicate MoS_2 particles appearing as dark stains or streaks.

NiMo(9)Y-3, although sample NiMo(5)Y-3 was slightly damaged.

The decrease of V_{mic} in NaY and HY-3 upon loading NiMo (Table 2) shows that NiMo species easily penetrated these Al-rich zeolites. This is neatly confirmed by EDX. The whole of the Ni–Mo species probably entered the NaY cavities since the secondary pore volume was unchanged. In zeolite HY-3, however, V_{sec} decreased somewhat, so that Ni and Mo ions were probably shared between the α cages and the mesopores.

Zeolite NiMo(9)Y-3 was markedly damaged upon sulfidation, especially at 673 K. The intensity ratio I_{533}/I_{331} and the V_{mic} agree with 10% extra-amorphization. This loss in crystallinity may be related mainly with dealumination of the framework since, according to the IR, 20% of the lattice Al was removed. This would also explain the decrease in a_o.

With zeolite HY-17, however, loading NiMo resulted in measurable dealumination, 25% amorphization, but only 10% loss in V_{mic} and nil in V_{sec}. Although the loss in V_{mic} nearly matches the volume of NiO + MoO_3, it is more likely to be the mere result of amorphization. On the other hand, zeolite NiMo(10)Y-17 appeared more resistant toward sulfiding. X-ray intensities establish the amount of extra amorphization at 4%. Here, the variations in internal volume are inconclusive since the decrease noted at 593 K was partly restored when sulfiding at 673 K.

In summary, the HY-3 and HY-17 supports behave differently, the latter being damaged mostly at the stage of NiMo introduction, the former at sulfidation. However, both catalysts retained at least 72% crystallinity after high temperature sulfiding.

2. *Distribution and Location of Ni and Mo*

The STEM-EDX results provided more insight into the homogeneity of Ni and Mo deposition and the location of the Ni and Mo species.

Oxidic NiMoY-3. In the A zones, Ni and Mo were invariably associated. As the Ni content matched the

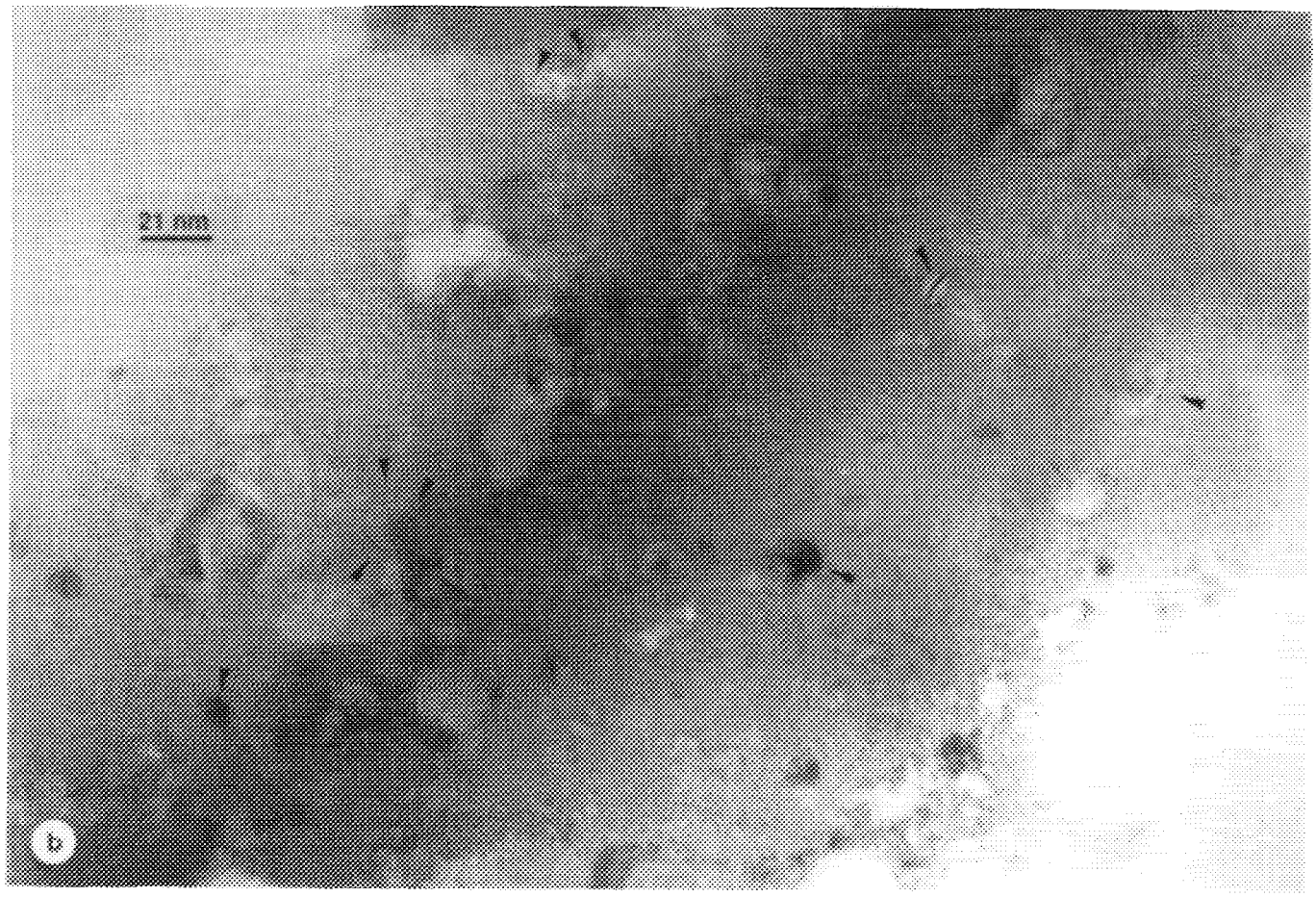

FIG. 5—*Continued*

chemical value, i.e., 3 at.%, the internal zones accounted for all of the Ni. The rather regular dispersion of Ni ions throughout the zeolite agrees with their location at cationic sites (30). By contrast, the Mo content was distinctly lower than the chemical one, especially in thin cuts. Then, only 50% of the Mo could penetrate the zeolite, the remaining being found as external MoO_3. Heterogeneities in internal Mo content suggest that this element occurs in both the primary and secondary pores. Interactions between Mo and Ni ions in the structural cavities were suspected by the increase of the unit-cell parameter a_0 (Table 2). The amount of such Mo could not be defined.

In the highly loaded NiMo(20)Y-3, the major part of Mo (67%) remained outside the zeolite. Similarly, the internal zones accounted for only half of the total nickel. Yet the two catalysts with 9 or 20 wt.% Mo were obtained from the same NiY-3 precursor. Hence, impregnation with an excess of molybdenum not only damaged the structure and texture of the zeolite, but also expelled some of the nickel previously introduced.

Sulfided NiMo(9)SY-3. As the MoS_2 particles in the A zones were smaller than the area swept by the EDX microprobe, their analysis contained a major contribution from the zeolite, and the A composition was again most frequent (Table 3). Sulforeduction hardly changed the amount of Mo within the zeolite (about 3 at.%). However, the Ni content dropped from 3% in zeolite NiMo(9)Y-3 to 1.3% in $NiMoS_l$(9)Y-3 and went as low as 0.9% in sample $NiMoS_h$(9)Y-3 sulfided at 673 K (Table 3). Therefore, the majority of the nickel was expelled. No Ni-rich phase, such as Ni_3S_2 (12), could be found in any domain.

The small MoS_2 particles appeared to be randomly distributed throughout the zeolite, including the clearer mesopores (Figs. 5a and b). However, the slabs parallel to the electron beam were preferentially found at the margin of a secondary pore. The bending of these MoS_2 slabs indicates a strong interaction with the HY-3 support, in a way reminiscent of Mo/Al_2O_3 catalysts (7, 8). The number and size of MoS_2 flakes detected by TEM, inside or at the surface of the zeolite, were too low to account for the 2.8 at.% Mo measured by EDX in the A zones. Some of the internal Mo should therefore exist as low condensed species or as particles too small to be detected ($d < 2$ nm).

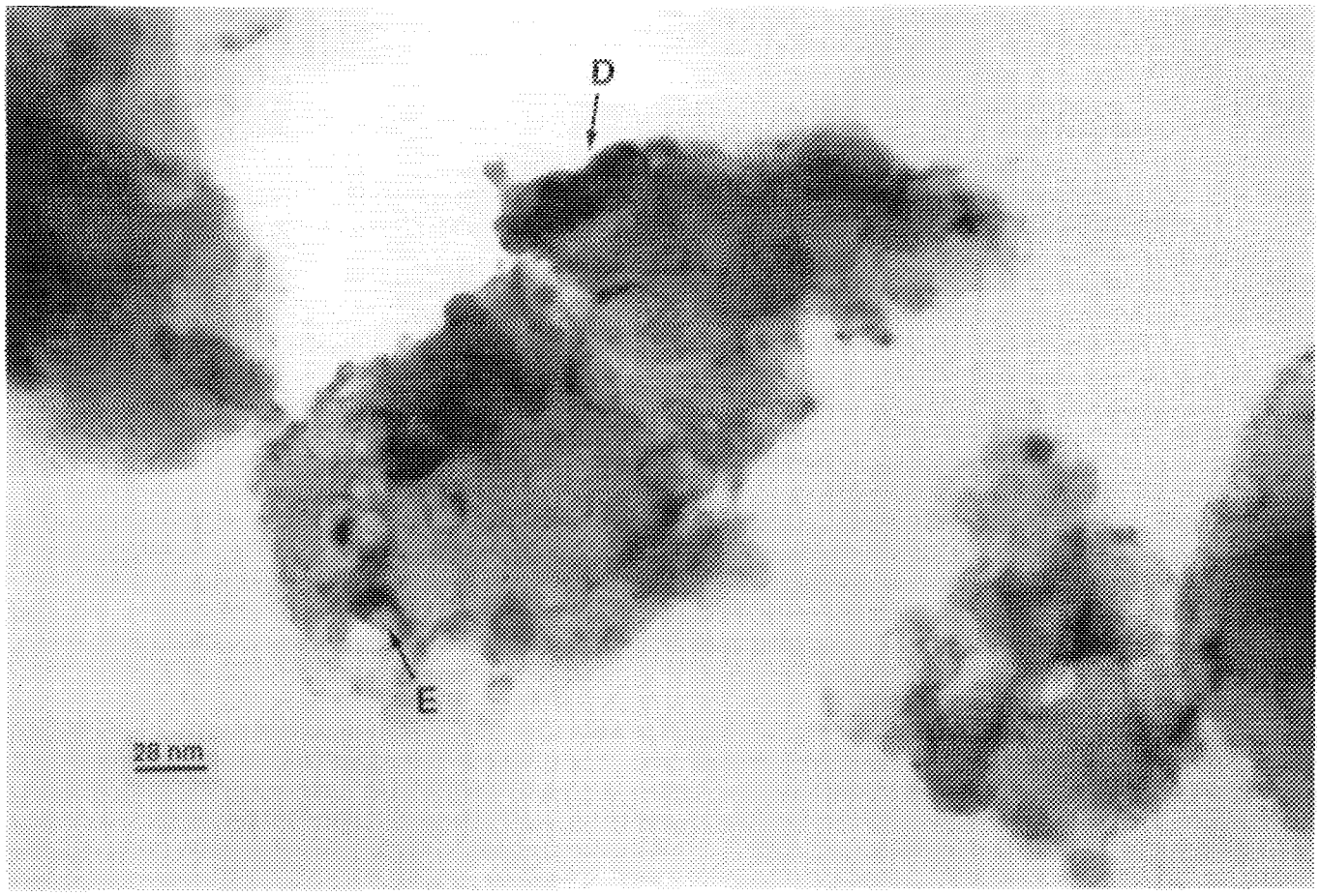

FIG. 6. TEM micrograph of NiMo(10)Y-17 catalyst particles, showing crystals of MoO_3 (D) and $NiMoO_4$ (E) identified by diffraction.

EDX indicated an overall S/Mo ratio equal to 1.1 at 593 K and 1.2 at 673 K. In the zeolitic A zones, the S/Mo ratio was only 1.2 at 593 K and rose to 1.8 at 673 K. Thus, the internal Mo and probably the Ni were not fully sulfided at 593 K, as previously evidenced by the IR of adsorbed CO (3). The inner ions were more extensively sulfided at 673 K, probably because migration was easier. Thus the low overall S/Mo mainly reflects an incomplete sulfidation of the external nodules of Mo oxide.

Moreover, the buildup of MoS_2 slabs within the zeolite structure probably induced local damage. Accordingly, amorphization was more pronounced at 673 K.

Oxidic NiMo(10)Y-17. In the NiMo(10)Y-17, the Si/Al ratio measured by EDX in the A zones was 29, which is above the overall ratio (Si/Al = 17) but close to the framework ratio measured by IR (R = 34.5). Hence, EDX confirmed that some lattice dealumination occurred in HY-17 upon loading NiMo, as was previously deduced from crystallinity and V_{mic} (Table 2). Nevertheless, only 2% of the lattice T (tetrahedral) atoms were extracted at this stage. No Al-rich domains could be localized.

The Ni and Mo contents measured by EDX in the A zones nearly matched the overall chemical composition (Table 4). Deviations were less than 25% for both metals. Therefore, at least 95% of the Ni and Mo ions penetrated the grains of HY-17. This is a major difference with zeolite HY-3, which could accommodate up to 3 at.% Ni, and no more than 3.3 at.% Mo. The exchange capacity of HY-17 does not exceed 1.2 at.% Ni, so that most of the Ni and Mo ions have to be accommodated in the secondary pores. Accordingly, the unit-cell parameter was unchanged, but the loss in crystallinity was 25% (Table 2).

Sulfided NiMo(10)SY-17. The larger number and size of the MoS_2 particles observed in sulfided NiMo(10)SY-17 as compared with NiMo(9)SY-3 show that sulfidation of the NiMo was easier in the former catalyst. This is confirmed by a higher sulfur level, for instance 6.8 at.% vs 5.9 at.% at 593 K. The difference may be related to the preferential deposition of the Ni and Mo ions in the mesopores of zeolite HY-17, where they are readily accessible to H_2S. Moreover, little damage occurred when the MoS_2 microparticles were built up.

Increasing the sulfidation temperature of NiMoY-17 results in a higher overall S/Mo ratio, from 1.10 to 1.34.

TABLE 4

EDX Analysis on Various Zones of NiMo(10)Y-17 Catalyst: Comparison of Averaged Compositions $\bar{c}$ with Bulk Chemical Composition

Analysis				Composition (at.%)				
Type	Zone	No. of analyses	Si/Al (at.%/at.%)	Si	Al	Ni	Mo	S
NiMo(10)Y-17 (calcined at 773 K)								
Chemical			16.8	85.9	5.1	2.4	6.6	0
EDX: thin cuts	A	8	29.4	88.1	3.0	2.3	6.6	0
	D	1	1.0	1.8	1.8	0.5	95.9	0
	E	4	1.6	3.9	2.4	32.7	61.0	0
NiMo(10)S_lY-17 (sulfided at 593 K)								
Chemical			17.0	80.0	4.7	2.3	6.2	6.8
EDX: thin cuts	A	10	14.7	83.8	5.7	1.2	5.4	3.9
	B	2	8.0	43.8	5.5	1.2	21.5	28.0
	D	1	8.5	15.3	1.8	1.0	27.0	54.9
NiMo(10)S_hY-17 (sulfided at 673 K)								
Chemical			17.2	78.9	4.6	2.2	6.1	8.2
EDX: thin cuts	A	10	29.3	84.9	2.9	1.0	4.3	6.9

The improvement is mainly at the benefit of internal Mo, as more MoS_2 slabs were observed by TEM. In addition, EDX indicated that the internal Mo content decreased somewhat upon sulfiding. Furthermore, the Ni content in the A zones dropped from 2.3 to 1.2 at.% upon sulfiding at 593 K and to 1 at.% at 673 K (Table 4).

Internal or external Ni and Mo. The percentages of metals staying within the grains are summarized in Table 5, together with the internal atomic ratios Ni/Mo. Whereas the HY-17 zeolite accommodates nearly all of the metals loaded, only half of the Mo can enter zeolite HY-3. Sulfidation provokes an extensive migration of the Ni and Mo ions inside or toward the outside of the zeolites. Eviction of Ni was common to both HY-3 and HY-17, especially at 673 K, but some Mo was also evicted from the HY-17. Finally, the internal Ni/Mo ratios were always lower than the overall chemical values: 0.49 in HY-3 and 0.36 in HY-17. However, they approached the optimal value 0.3 claimed for $NiMo/Al_2O_3$ catalysts (31).

Relevance to catalysis. As already pointed out, the

TABLE 5

Proportion (%) of Ni and Mo inside the Zeolites at Different Stages: Oxided, Sulfided at 593 K (S_l) or at 673 K (S_h)

Catalyst activation	NiMo(9)HY-3			NiMo(10)HY-17		
	Oxided	S_l	S_h	Oxided	S_l	S_h
Fraction of metal inside the zeolite (from EDX analysis of the A zones)						
Internal Ni (%)	>95	43	33	>95	50	42
Internal Mo (%)	53	46	48	>95	83	61
Ni/Mo (at.%/at.%)	0.91	0.46	0.32	0.34	0.22	0.23
Rates of reaction (mol h^{-1} kg^{-1})[a] and turnover frequencies for Hp						
Be Rate ($\times 10^2$)	—	4.8	3.5	—	5.6	9.7
Hp Rate	—	2.7	5.2	—	0.6	0.9
Hp TOF (h^{-1})[b]	—	1.4	3.2	—	1.9	2.9

Note. Reaction rates measured at 553 K for benzene hydrogenation (Be rate) and *n*-heptane hydroconversion (Hp rate). Uncertainties are ±0.01 for Be and ±0.3 for Hp, in units of mol h^{-1} kg^{-1}.

[a] Uncertainties on rates are ±0.01 for Be and ±0.3 for Hp in units of mol h^{-1} kg^{-1}.

[b] Based on numbers of lattice Al.

FIG. 7. TEM images of thin cuts in catalysts: (a) NiMo(10)S_lY-17 (sulfided at 593 K); (b) NiMo(10)S_hY-17 (sulfided at 673 K). Arrowheads show some MoS_2 microparticles.

nearly equal rates of hydrogenation measured over sulfided $NiMo/Al_2O_3$ and NiMo/HY mean that comparable dispersion of the NiMo sulfide was achieved on both kinds of support. The new feature is the discovery of a large fraction of the Ni and Mo, 50% in NiMoSY-3, at the outside of the sulfided zeolites, in the form of bulky nodules. Thus catalytic activity relies essentially on the NiMo species inside the zeolite.

TEM images revealed exceptionally small particles of MoS_2 within the zeolites after sulfidation at 593 K. When the sulfidation was performed at 673 K, the particles grew larger and Mo dispersion seemed to decrease, but at the same time more Mo ions were sulfided (Tables 3 and 4). The result was an enhancement in hydrogenation and also in hydrocracking activity. With catalyst NiMoSY-3, the enhancement could not be observed directly with benzene, but was obvious with heptane (Table 5).

The two NiMoSY catalysts have similar hydrogenation capacities, and the higher rate of heptane conversion observed with NiMoSY-3 (Table 5) mainly reflects a higher density of acid sites.

Hydrocracking obeys the classical bifunctional mechanism, which may be simplified as follows:

(a) dehydrogenation:

$$n\text{-alkane } (n\text{-P}) \rightleftharpoons n\text{-alkene } (n\text{-O}) + H_2$$

(b) protonation:

$$n\text{-O} + H^+ \rightleftharpoons n\text{-P}^+ \text{ a linear carbenium ion}$$

(c) isomerization:

$$n\text{-P}^+ \rightleftharpoons i\text{-P}^+ \text{ a branched carbenium ion}$$

(d) desorption of isomer:

$$i\text{-P}^+ + n\text{-O} \overset{k_d}{\rightleftharpoons} n\text{-P}^+ + i\text{-O a branched alkene}$$

or

(e) cracking:

$$i\text{-P}^+ \xrightarrow{k_c} \text{cracked products.}$$

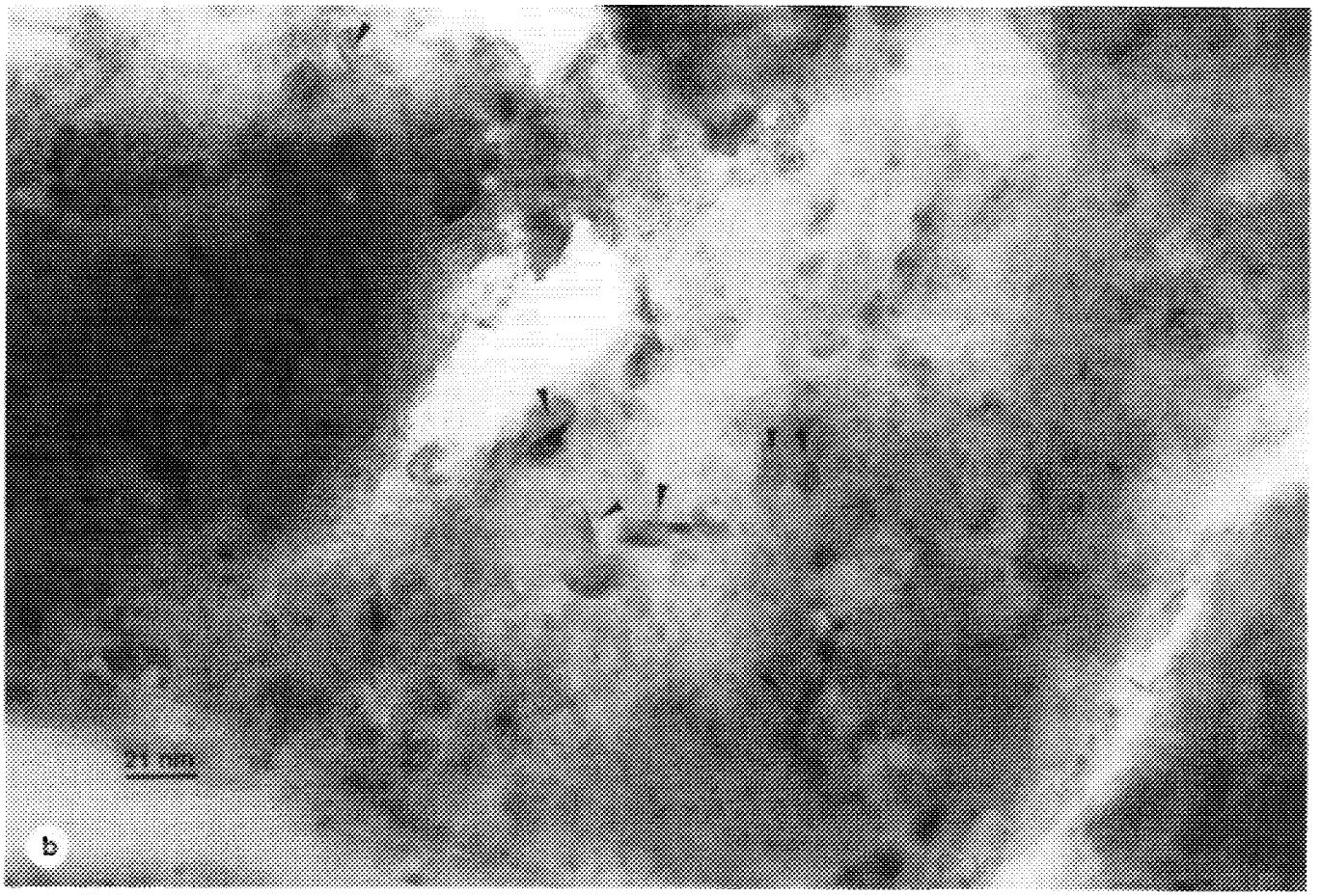

FIG. 7—*Continued*

The rates of the last two steps involve the carbenium ion concentration [i-P^+]. Hence, the overall rate of hydrocracking appears proportional to the density of acid sites. The rates reported in Table 5 comply with this, as turnover frequencies based on the density of acid sites were rather close for both NiMo zeolites.

Nevertheless, the selectivity to heptane isomers was found to be much lower than with Pt-containing zeolites, where it may reach 70% at 600 K (32). Indeed, if the zeolites provide a good dispersion and accessibility of the NiMo sulfide, the hydrogenation function is insufficient to allow ideal hydrocracking of heptane (32). The dehydrogenation step (a) stays far under equilibrium, resulting in a low alkene concentration [n-O]. This makes the desorption of isomers (step d) rather slow and the lifetime of the branched carbenium ions comparatively long. Therefore, cracking (step e) becomes favored, explaining the poor selectivity.

Catalyst NiMoSY-17 was expected to be more selective than the more acidic NiMoSY-3 (31). Actually, this was not the case. The selectivity for isomers depends on the relative rates of steps (d) and (e), i.e., the ratio $r_d/r_e = k_d[n\text{-O}]/k_e$.

The rate constants k_d and k_e depend only on the strength of the acid sites and should be similar for two catalysts having equal turnover numbers. Therefore, the selectivity is governed only by the concentration of alkenes at the acid sites. If transport limitations were absent, catalysts with comparable hydrogenation capacities should have the same selectivity.

As the selectivity of catalyst NiMoSY-17 was slightly under that of NiMoSY-3, we might suspect a slow transport of the alkene from the metallic to the acidic sites. Indeed, the average distance between both kinds of sites is particularly long in zeolite HY-17. However, transport limitations do not appear to be drastic. Besides, the long distance between sites favors coking, which may in turn affect the selectivity.

According to the heptane test, there is no advantage in decreasing the acidity of the zeolite by dealumination. The

balance between both acid and hydrogenation functions is not improved. The hydrogenation activity of the sulfide NiMo stays too low despite its apparent good dispersion.

CONCLUSIONS

Ni ions are readily introduced into HY zeolites, where they reach first the cationic sites, then the mesopores. The amount of Mo which can be fitted into HY-3 is limited to 3.3 at.%, as MoO_3 and aluminate are detected outside of the zeolite. More Mo can penetrate zeolite HY-17 owing to its large secondary pore volume.

In the sulfided catalysts, flake-shaped MoS_2 microparticles are observed in the mesopores. The density of flakes is higher on HY-17 than on HY-3. Sulfidation evicts 50% of the Ni from both zeolites and also some of the Mo.

The NiMo zeolites sulfided at 593 K nearly match the activity of $NiMo/Al_2O_3$ for benzene hydrogenation. Sulfiding at 673 K enhances their activity for hydrogenation and also for heptane hydrocracking. In the latter reaction, the NiMoY-17 is much less active than the NiMoY-3, due to a lower density of acid sites. The NiMo sulfides loaded into zeolites do not have sufficient hydrogenation capacity to induce a high selectivity for isomerization of heptane.

ACKNOWLEDGMENTS

The help of Mrs. P. Beaunier and Mr. M. Lavergne for the TEM and STEM-EDX measurements is greatly appreciated.

REFERENCES

1. Dohler, W., *in* "Proceedings, 8th International Congress on Catalysis, Berlin, 1984," Vol. III, p. 499. Dechema, Frankfurt-am-Main, 1984.
2. Dufresne, P., Quesada-Perez, A. M., and Mignard, S., *in* "Catalysis in Petroleum Refining" (D. L. Trimm, Ed.), p. 301. Elsevier, Amsterdam, 1989.
3. Leglise, J., Janin, A., Lavalley, J. C., and Cornet, D., *J. Catal.* **114,** 388 (1988).
4. Leglise, J., El Qotbi, M., Goupil, J. M., and Cornet, D., *Catal. Lett.* **10,** 103 (1991).
5. Leglise, J., El Qotbi, M., and Cornet, D., *Collect. Czech. Chem. Commun.* **57,** 882 (1992).
6. Sanders, J. V., and Pratt, K. C., *J. Catal.* **67,** 331 (1981).
7. Delannay, F., *Appl. Catal.* **16,** 135 (1985).
8. Eijsbouts, S., Heinerman, J. J. L., and Helzerman, H. J. W., *Appl. Catal. A* **105,** 53 (1993).
9. Hayden, T. F., Dumesic, J. A., Sherwood, R. D., and Baker, R. T. K., *J. Catal.* **105,** 299 (1987).
10. Pratt, K. C., Sanders, J. V., and Christov, V., *J. Catal.* **124,** 416 (1990).
11. Ryan, R. C., Kemp, R. A., Smegal, J. A., Denley, D. R., and Spinnler, G. E., *in* "Hydrotreating Catalysts—Preparation, Characterization and Performance: Proceedings of the Annual International AIChE Meeting, Washington, DC, Nov. 27 to Dec. 2, 1988" (M. L. Occelli and R. G. Antony, Eds.), p. 21, Studies in Surface Science and Catalysis, Vol. 50. Elsevier, Amsterdam, 1989.
12. Smith, B. J., and Wei, J., *J. Catal.* **132,** 21 (1991).
13. Sørensen, O., Clausen, B. S., Candia, R., and Topsøe, H., *Appl. Catal.* **13,** 363 (1985).
14. Van Doorn, J., Moulijn, J. A., and Djega-Mariadassou, G., *Appl. Catal.* **63,** 77 (1990).
15. Srinivasan, S., Datye, A. K., and Peden, C. H. F., *J. Catal.* **137,** 513 (1992).
16. Cruz-Reyes, J., Avalos-Borja, M., Farias, M. H., and Fuentes, S., *J. Catal.* **137,** 232 (1992).
17. Ezzamarty, A., Catherine, E., Hémidy, J. F., Janin, A., Lavalley, J. C. Leglise, J., and Mériaudeau, P., *in* "Zeolites: Facts, Figures, Future" (P. A. Jacobs and R. A. Van Santen, Eds.), part B, p. 1025, Studies in Surface Science and Catalysis, Vol. 49. Elsevier, Amsterdam, 1989.
18. Spiridinova, N. L., Spiridinov, S. E., Khadjiev, S., Machinskaia, M. E., and Kosolapova, A. P., *Kinet. Katal.* **30,** 1005 (1980).
19. A. S. T. M. D. 3906-80, Philadelphia, PA, 1980.
20. Klug, H. P., and Alexander, L. E., *in* "X-Ray Diffraction Procedures." Wiley, New York, 1954.
21. Johnson, M. F. L., *J. Catal.* **52,** 425 (1978).
22. Cid, R., Gil Llambias, F. J., Fierro, J. L. G., López-Agudo, A., and Villasenor, J., *J. Catal.* **89,** 478 (1984).
23. Fierro, J. L. G., Conesa, J. C., and López-Agudo, A., *J. Catal.* **108,** 334 (1987).
24. Cid, R., Orellana, F., and López-Agudo, A., *Appl. Catal.* **32,** 327 (1987).
25. Laniecki, M., and Zmercziak, W., *Zeolites* **11,** 18 (1991).
26. Choi-Feng, C., Hall, J. B., Huggins, B. J., and Beyerlein, R. A., *J. Catal.* **140,** 395 (1993).
27. Gallezot, P., Feron, B., Bourgogne, M., and Engelhard, P., *in* "Zeolites: Facts, Figures, Future" (P. A. Jacobs and R. A. Van Santen, Eds.), p. 1281, Studies in Surface Science and Catalysis, Vol. 49, Elsevier, Amsterdam, 1989.
28. Aouli, L., Jeanjean, J., Dereigne, A., Tougne, P., and Delafosse, D., *Zeolites* **8,** 517 (1988).
29. Lynch, J., Raatz, F., and Dufresne, P., *Zeolites* **7,** 333 (1987).
30. Delahaie, S., Chambellan, A., Cornet, D., and Hémidy, J. F., *in* "Perspectives in Molecular Sieve Science" (W. H. Flank and T. E. Whyte Jr., Eds.), p. 579, ACS Symposium Series, Vol. 368. American Chemical Society, Washington, DC, 1989.
31. Le Page, J. F., Cosyns, J., Courty, P., Freund, E., Franck, J. P., Jacquin, Y., Juguin, B., Marcilly, C., Martino, G., Miquel, J., Montarnal, R., Sugier, A., and van Landeghem, H., *in* "Applied Heterogeneous Catalysis." Technip, Paris, 1987.
32. Weitkamp, J., *in* "Hydrocracking and Hydrotreating" (J. W. Ward, Ed.), p. 1, ACS Symposium Series, Vol. 20. American Chemical Society, Washington, DC, 1975.